Aluminum-Doped Magnesium-Manganese Mixed Nano Ferrites: An Effective Photocatalyst for Methylene Blue

[1*]Dr. M. S. Sameem, [2]Dr. B. Gowri Shannkari, [3]Dr. K. S. Balamurugan, [4]Dr. G. Srihari,

[1*]Assistant Professor, Department of Chemistry, M.S.S.Wakf Board College, K.K.Nagar, Madurai, Tamilnadu, India

[2]Assistant Professor, PG and Research Department of Chemistry, Saraswathi Narayanan College (Autonomous), Madurai, Tamilnadu, India

[3]Professor & Head, Department of Electronics and Communication Engineering, Karpaga Vinayaga College of Engineering and Technology, Chengalpattu,

[4]Professor & Head, Department of Electronics and Communication Engineering, K.S.R.M College of Engineering, Kadapa, Anthra Pradesh, India.

Abstract

The present research synthesizes an Al^{3+}-doped $Mg_{0.50}Mn_{0.50}Al_xFe_{2-x}O_4$ spinel ferrite system (x = 0.25, 0.50, 0.75) using a modified auto combustion process. These nano ferrites' structural, magnetic, and optical characteristics are investigated using a variety of techniques, including EDAX, SEM, XRD, FTIR, DLS, M-H loop, and UV-DRS. The dye degradation studies for methylene blue employing nano ferrites are carried out under sun radiation in the presence of H_2O_2, and the absorbance is measured in a UV-visible spectrophotometer for the varied specimens/concentrations. Among all the specimens, 0.25 Al^{3+}-doped magnesium-manganese nano ferrite degraded the most methylene blue dye in 75 minutes with the least amount of H_2O_2.

Introduction

Spinel ferrite nanoparticles have a face-centered-cubic structure defined by (M^{2+}) $[Fe^{3+}]_2O_4$, with two interpenetrating sublattices: tetrahedral site (A) and octahedral site [B], which differ in their structural and magnetic properties. They are promising materials for various applications due to their nontoxic nature and imposing photocatalytic, magnetic, and electronic properties [1]. Because of the nanoscale regime and huge surface area, spinel ferrites with 3+ cations substitution can alter their physical characteristics and improve photocatalytic processes [1, 2]. The literature describes numerous synthesis strategies for producing manganese ferrite, magnesium ferrite, and magnesium-manganese nanoferrites [3-23]. These magnetic ferrites have a wide range of applications, including wastewater treatment, photocatalysis, methylene blue (MB) dye degradation in the presence of hydrogen peroxide, magnetic resonance imaging, novel

magnetic hyperthermia agents, cardiovascular effect, supercapacitors, controlled drug delivery, antimicrobial activity, sbioanalytical field, voltametric sensor, supercapacitor, hyperthermia application, anode material for a lithium battery, dye degradation, LPG sensor, microwave absorption, biomedical applications, and electromagnet [24-43]. MB dye is used in many different sectors; among them, the textile industry has long used MB dyes as a well-liked apparel colourant [44]. Massive amounts of effluent from MB dye-related companies are constantly released into natural water sources [44, 45]. Because of its extreme toxicity, MB dye is harmful to human health above a certain ppm concentration.

As a result, it poses a serious threat to the ecological environment and has been linked to a number of serious health issues in humans, such as blindness, respiratory distress, abdominal, mental, and digestive disorders, jaundice, and so on. As a result, it is critical to purify the vast amounts of water required for human consumption. To do this, an efficient and reasonably priced material must be developed in order to remove MB and even other dyes from wastewater, refresh the environment, and enable the provision of pure drinking water to people [44]. It has been discovered that photodegradation of MB dye in the presence of sunlight is an affordable and environmentally beneficial method of MB dye degradation. A review of the literature demonstrates the use of different spinel nano ferrites in photocatalytic dye degradation for wastewater treatment. AlBassami et al. report that the ideal composition for Co-Mn-Zn spinel ferrites is Co-content = 0.2, and that this composition strongly depends on bandgap composition [46]. Mostafa et al. [47] report a study of Mo-substituted magnesium nano ferrite, which demonstrates photocatalytic activity due to increased surface area and structural defects that prevent electron-hole recombination. When compared to the untreated sample's degrading efficiency of 74%, Naz et al. [48] claim that the Mn-nano ferrite treated with plasma had an improved efficiency of up to 91%. Using Ni–Cu ferrite, Pan et al. [49] examine the impact of composition and pH on the removal of MB dye. They find that at pH_5, $Ni_{0.5}Cu_{0.5}Fe_2O_4$ provided the highest level of MB dye removal efficiency. Therefore, the composition, synthesis conditions, particle size, and other factors of spinel ferrites influence their structural and magnetic characteristics, which may then be efficiently utilized for the photocatalytic destruction of dyes for the goal of purifying water. Therefore, replacement in different ferrite compositions would result in an impending new class of materials that would be more suited for applications involving water purification [50–56].

Because Al^{3+}-doped magnesium–manganese nano ferrites ($Mg_{0.50}Mn_{0.50}Al_xFe_{2-x}O_4$, x = 0.25, 0.50, 0.75) exhibit tiny band gap energies and strong photocatalytic activity, we describe photocatalytic degradation of MB utilizing these ferrites in the current study [57]. Every sample was created using the modified auto combustion technique. Energy dispersive analysis of x-rays (EDAX), dynamic light scattering experiment (DLS), scanning electron microscopy (SEM), vibrating sample magnetometer (VSM) measurements, Fourier transform infrared spectroscopy (FTIR), x-ray diffraction analysis (XRD), and UV–visible diffuse reflectance spectroscopy were used to characterize the synthesized samples. Using hydrogen peroxide and loading the obtained nano ferrites, the photocatalytic activity of the prepared spinel ferrite samples was examined in the presence of sunshine. The absorbance was measured using a UV–visible spectrophotometer to assess the MB degradation for the same.

Experimental Analyses

A modified auto combustion process was used to create three specimens of aluminum-doped magnesium-manganese nano ferrites, or $Mg_{0.50}Mn_{0.50}Al_xFe_{2-x}O_4$, x = 0.25, 0.50, 0.75). The precursors for this process included urea, magnesium nitrate hexahydrate, manganese nitrate tetrahydrate, ferric nitrate nonahydrate, aluminium nitrate nonahydrate, and distilled water. In this case, the propellant chemistry approach was utilized to calculate the stoichiometric percentage [58]. In a Pyrex bowl, 40 millilitres of distilled water were used to dissolve each precursor. This Pyrex dish was placed in a 300°C muffle furnace that had been warmed. After 30 minutes, the combustion took place in the furnace.

Samples were allowed to cool overnight in the boiler. To create fine ferrite nanoparticles, the samples were removed and pounded for six hours with an agate mortar and pestle. Utilizing CuKα radiation (wavelength: 0.15406 nm), the Philips X'pert MPD System was utilized to get XRD data at room temperature at a count per step of 0.02 per second. Scherrer's grain diameter and the lattice parameter were determined by analyzing the XRD data. Using the conventional approach, XRD peak intensities were used to assess the cationic distribution of synthesized specimens [59]. Cationic distribution, which is sensitive to variations in the cationic distribution as mentioned in ref. [59], is achieved by matching the calculated, experimental intensity ratios for the (422), (400), and (220) planes. We find that the intensity ratios $I_{(220)}/I_{(440)}$, $I_{(400)}/I_{(422)}$, and $I_{(220)}/I_{(400)}$ vary for different cation distribution on A and B sites. It is assumed that the optimal cation distribution between sites A and B is the one for which there is a discernible

agreement between the theoretical and experimental ratios I_{hkl}^{Obs}. and I_{hkl}^{Calc} of the observed and calculated intensities. To find the IR absorption bands and force constants, Thermo Scientific FTIR measurements in absorption mode were performed (inside a KBr matrix).

Quantitative analysis, particle size distribution, and surface morphology were obtained using an energy dispersive spectrometer (EDS) and a Zeiss SEM. DLS was used to measure the particle size and particle size distribution at 25°C using Microtrac Nanotrac Flex. Hysteresis loops were obtained using a room-temperature vibrating sample magnetometer (VSM). Hysteresis experiments yielded saturation magnetization (M_s), coercivity (H_c), and decreased remanence (M_r/M_s). With the use of UV–visible diffuse reflectance spectroscopy, band gap energies were determined. The MB to H_2O_2 ratio in the current study was set at 9:1. To break down the MB dye, several combinations of 20 mg synthesized nano ferrites + MB and H_2O_2 solutions were exposed to sunshine. The identical combinations were also utilized in the deterioration test and light absorption measurements in the UV-visible spectrophotometer. There is another explanation of the entire experiment here [43]. The effects of catalyst dose and MB concentration were also examined in the current study project.

Results Analyses

XRD

The XRD pattern of the Al^{3+}-doped Mg–Mn micro ferrites under study is displayed in Figure 1. The cation distribution of the synthesized nano ferrites was ascertained [60–64], as stated in Table 1, as a result of all the diffraction peaks for the nano ferrites being properly indexed, which confirmed the creation of the spinel phase. Figure 1 shows a few Braggs' reflection peaks of unreacted Fe_2O_3 that happened throughout the synthesis process. Using the Debye-Scherrer formula, the crystallite size of the synthesized nano ferrites was determined and is reported in Table 4 (with a range of 35 to 42 nm) [60-63]. As was previously noted in previous investigations with comparable compositions [65], the lattice parameter for the examined materials was 0.8379, 0.8385, and 0.8397 nm, respectively, for samples with Al-content 0.25, 0.50, and 0.75. Table 1 illustrates how increasing the lattice parameter with Al^{3+} substitution causes an expansion of the unit cell, which may be attributed to changes in the cationic distribution brought on by replacement.

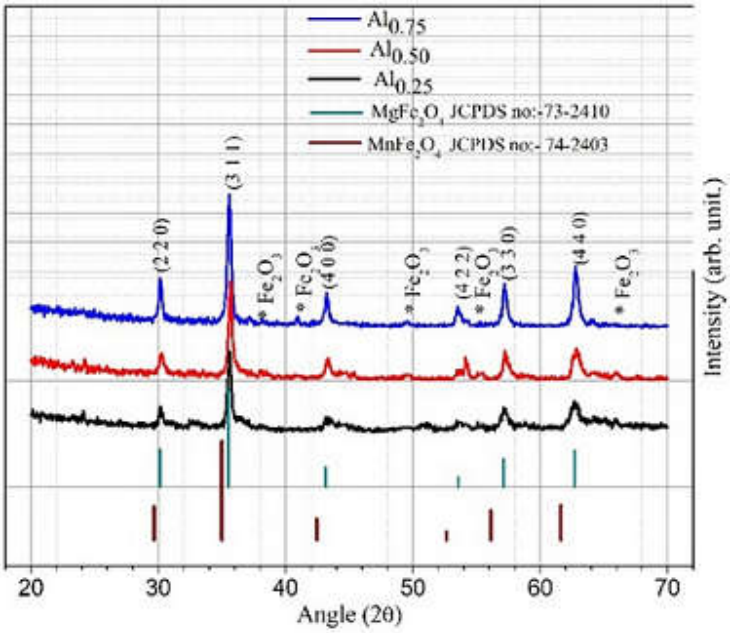

Figure 1 XRD pattern of $Mg_{0.50}Mn_{0.50}Al_xFe_{2-x}O_4$ (x = 0.25, 0.50, 0.75) compared with standard JCDPS patterns of $MgFe_2O_4$ and $MnFe_2O_4$

Table 1 indicates that Fe^{3+}, Mg^{2+}, and Mn^{2+} ions are present on both A and B sites. The concentration of Fe^{3+} ions decreases with each additional Al addition, while (i) Mn^{2+} ions continue to be more prevalent on B-site than A-site, (ii) Mg^{2+} ions continue to be more prevalent on A-site than B-site, and (iii) all of the Al^{3+} ions are present on B-site.

Table 1 Cation distribution of synthesized ferrites, and calculated and observed values of intensity ratios I_{220}/I_{440}, I_{400}/I_{422}, and I_{220}/I_{440}

Cation distribution	**Intensity ratio**					
	I_{220}/I_{440}		**I_{400}/ I_{422}**		**I_{220}/I_{440}**	
	Calc.	**Obs.**	**Calc.**	**Obs.**	**Calc.**	**Obs.**
$(Mg^{2+}_{0.18}\ Mn^{2+}_{0.18}Fe^{3+}_{0.64})_A$ $[Mg^{2+}_{0.32}\ Mn^{2+}_{0.32}Al^{3+}_{0.25}Fe^{3+}_{1.11}]_BO^{2-}_4$	0.903	0.890	1.504	1.491	2.881	2.658
$(Mg^{2+}_{0.21}\ Mn^{2+}_{0.20}Fe^{3+}_{0.59})_A$ $[Mg^{2+}_{0.29}\ Mn^{2+}_{0.30}Al^{3+}_{0.50}Fe^{3+}_{0.91}]_BO^{2-}_4$	0.921	0.902	1.651	1.521	2.912	2.692
$(Mg^{2+}_{0.23}\ Mn^{2+}_{0.22}Fe^{3+}_{0.55})_A$ $[Mg^{2+}_{0.27}\ Mn^{2+}_{0.28}Al^{3+}_{0.75}Fe^{3+}_{0.62}]_BO^{2-}_4$	0.939	0.912	1.682	1.556	2.923	2.758

The computed cationic distribution's dependability is confirmed by the close agreement of the intensity ratios of I_{220}/I_{440}, I_{400}/I_{422}, and I_{220}/I_{440} (see Table 1) with their observed (Obs.) counterparts.

EDAX

Using EDAX mapping, the compositional stoichiometry of the magnesium-manganese micro ferrite doped with aluminium is investigated. All of the elements—Al, Mn, Mg, Fe, and O—as well as their uniform allocation and the formation of the desired ferrite phase are confirmed by representative EDAX. Figure 2 displays the EDAX pattern of magnesium-manganese mixed ferrite ($Mg_{0.50}Mn_{0.50}Al_{0.25}Fe_{1.75}O_4$) doped with aluminium. The EDAX findings show that the suggested synthesis process was successful in producing the necessary ferrite materials. Other synthetic nano ferrites have comparable results. As seen in Table 2, there is not a single trace of any contaminant in these specimens.

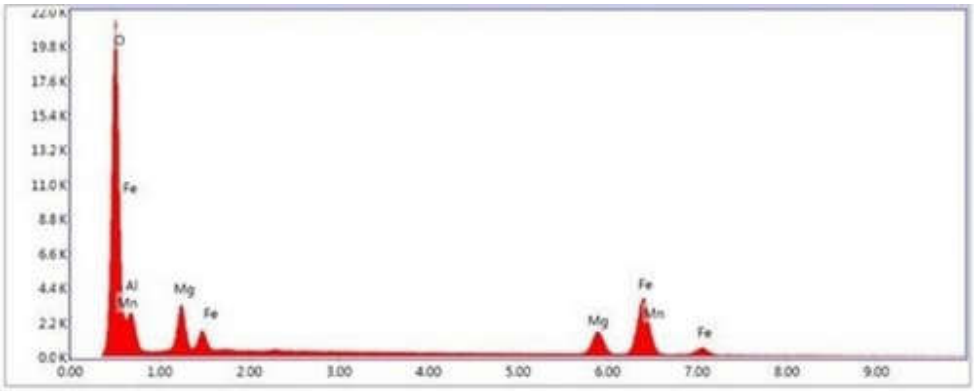

Figure 2 Typical EDAX pattern of $Mg_{0.5}Mn_{0.5}Al_{0.25}Fe_{1.75}O_4$

The typical SEM picture (see Figure 3a) of $Mg_{0.50}Mn_{0.50}Al_{0.25}Fe_{1.75}O_4$ shows that the grains are not distributed uniformly, which may be related to the emission of toxic gases during the synthesis process, resulting in a fractured surface with voids and pores. The estimated particle size is 34.28 nm, and the distribution width is 4.14 nm. The particle size distribution is displayed in Figure 3b.

FTIR Spectroscopy

With the use of FTIR spectroscopy, the molecular and chemical makeup of synthetic spinel ferrite is ascertained. As seen in Figure 4, for spinel ferrite specimens, there are two designated absorption bands, $\boldsymbol{\upsilon_1}$ (about 600 cm^{-1}) and $\boldsymbol{\upsilon}_2$ (approximately 400 cm^{-1}), which appeared owing to tetrahedral and octahedral sites, respectively.

Table 2 Result of EDAX characterization for aluminum-doped magnesium–manganese mixed ferrite ($Mg_{0.50}Mn_{0.50}Al_xFe_{2-x}O_4$)

Content X	Element present	Compositions in atomic percentage (at %) using EDAX
0.25	Mg	8.58
	Mn	9.54
	Al	8.57
	Fe	31.41
	O	41.90
0.50	Mg	9.88
	Mn	10.11
	Al	14.15
	Fe	29.45
	O	36.41
0.75	Mg	11.33
	Mn	13.32
	Al	21.24
	Fe	28.41
	O	25.70

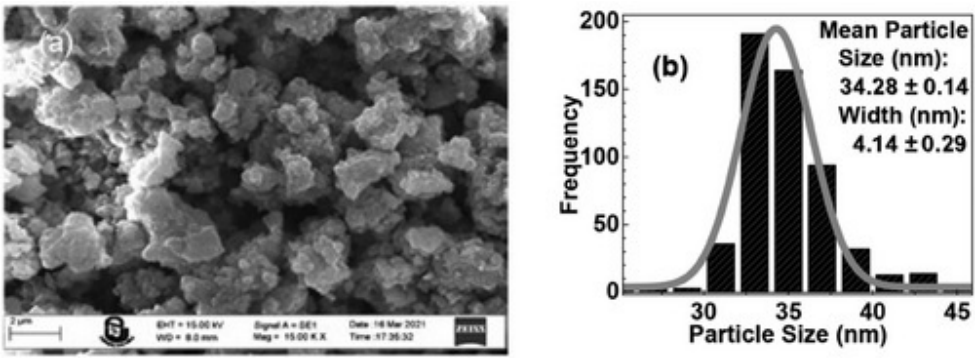

Figure 3 (a) SEM images of the $Mg_{0.50}Mn_{0.50}Al_{0.25}Fe_{1.75}O_4$ specimen, (b) particle size distribution

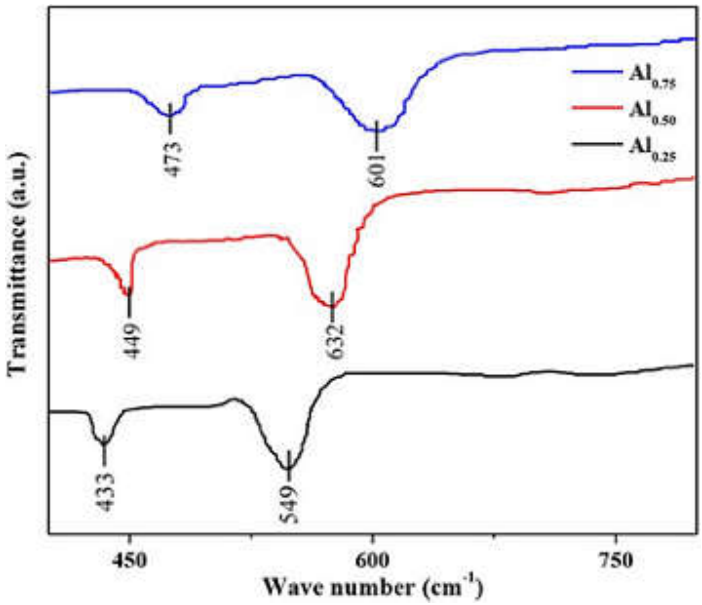

Figure 4 FTIR spectra of $Mg_{0.5}Mn_{0.5}Al_xFe_{2-x}O_4$ (x = 0.25, 0.50, 0.75) system

Table 3 Various parameters of FTIR of synthesized specimens

Sample	Molecular weight (g mol^{-1})	υ_1 (cm^{-1})	υ_2 (cm^{-1})	k_t (N m^{-1})	k_o (Nm^{-1})
$Mg_{0.50}Mn_{0.50}Al_{0.25}Fe_{1.75}O_4$	207.78	549	443	114.84	93.67
$Mg_{0.50}Mn_{0.50}Al_{0.50}Fe_{1.50}O_4$	200.60	573	449	122.69	92.71
$Mg_{0.50}Mn_{0.50}Al_{0.75}Fe_{1.25}O_4$	193.47	601	473	133.21	91.24

The force constants for both systems are computed using conventional formulas and absorption bands, and they are shown in Table 3 [61].The presence of nonmagnetic Al^{3+} at octahedral sites replacing iron content has been seen to cause a drop in octahedral force constants in magnesium–manganese nano ferrites as the Al^{3+} content rises. This may have an increasing trend on tetrahedral force constants. The fluctuation in the length of the cation-oxygen bond can be attributed to this [66].

Dynamic Light Scattering Experiment

The DLS experiment measures the particle sizes of all synthesized nanoparticles. Typically, measurements are made of the nanoparticles' hydrodynamic diameter, which may be significant for bacteriostatic purposes [67]. The hydrodynamic size distribution of $Mg_{0.50}Mn_{0.50}Al_{0.25}Fe_{1.75}O_4$ is seen in Figure 5. Other synthetic nano ferrites have comparable results. Table 4 lists the particle size from the DLS measurement and the crystallite size

computed from the XRD for comparison's sake. The DLS experiment's higher particle size can be attributed to the nano ferrites' insolubility and agglomeration in water. Raje Sheikh et al. achieved similar outcomes using autoignition synthesis to create Ni–Zn ferrite doped with rare-earth metals [68].

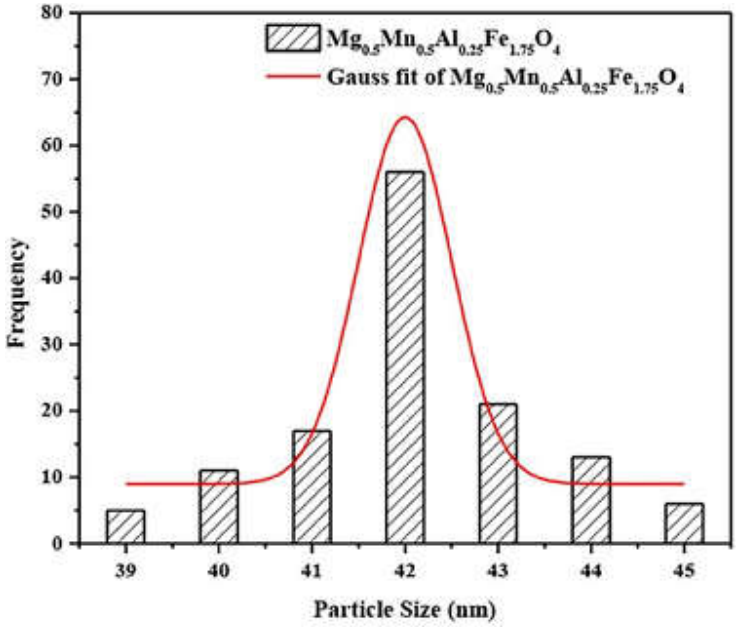

Figure 5 Particle size from DLS measurement of $Mg_{0.50}Mn_{0.50}Al_{0.25}Fe_{1.75}O_4$

Table 4 Crystallite size from XRD and particle size from DLS measurement

Sample	Crystallite size from XRD (nm) (±0.05 nm)	Particle size from DLS (nm) (±0.5 nm)
$Mg_{0.50}Mn_{0.50}Al_{0.25}Fe_{1.75}O_4$	38.52	42.3
$Mg_{0.50}Mn_{0.50}Al_{0.50}Fe_{1.50}O_4$	39.72	44.4
$Mg_{0.50}Mn_{0.50}Al_{0.75}Fe_{1.25}O_4$	41.50	47.3

MH Hysteresis Loops of Synthesized Ferrites

All prepared specimens' hysteresis loops measured at 300 K and with a maximum applied field of 10 kOe, are displayed in Figure 6. Table 5 lists the several magnetic properties of micro ferrites that are measured by the MH loop. Perusal of hysteresis loops shows a decrease of saturation magnetization (see Figure 6b) with increasing Al^{3+} content, is ascribable to the replacement of magnetic cations by nonmagnetic cations, and is consistent with earlier studies with similar compositions [1, 63, 69].

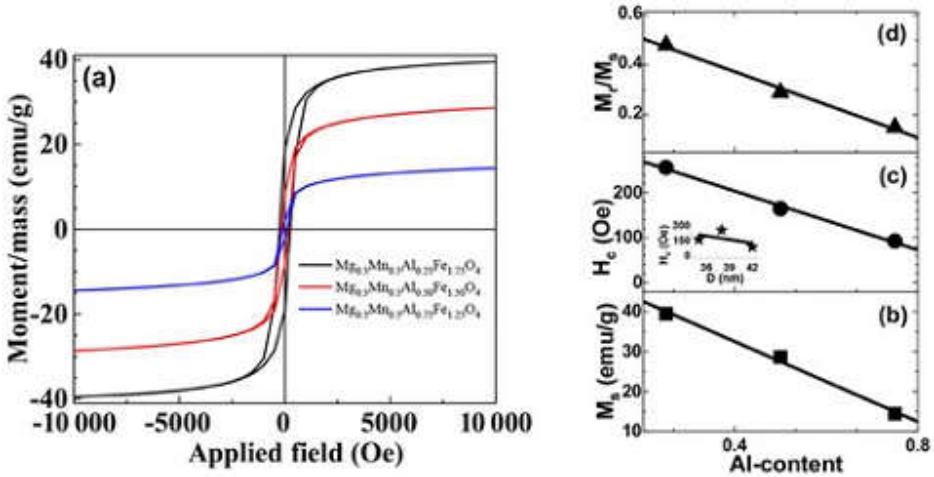

Figure 6 (a) Hysteresis loops of the studied samples: for $Mg_{0.05}Mn_{0.50}Al_xFe_{2-x}O_4$ (x = 0.25, 0.50, 0.75), and (b–d) respectively show Al-content dependence of M_s, H_c (Inset: variation of H_c with D, continuous line in guide to the eye), and M_r/M_s. Continuous lines are linear fit to the data

Table 5 Saturation magnetization (M_s), coercive field (H_c), remanent magnetization (M_r), and squareness ratio (M_r/M_s) of synthesized nano ferrites

Composition	M_s (emu g^{-1})	H_c (Oe)	M_r (emu g^{-1})	M_r/M_s
$Mg_{0.50}Mn_{0.5}Al_{0.25}Fe_{1.75}O_4$	39.50	256	19.04	0.48
$Mg_{0.50}Mn_{0.5}Al_{0.50}Fe_{1.50}O_4$	28.60	164	8.34	0.29
$Mg_{0.50}Mn_{0.5}Al_{0.75}Fe_{1.25}O_4$	14.40	92	2.11	0.15

Grain diameter observations are consistent with the reduction in coercivity with increasing Al-content [69]. A drop in the squareness ratio as the Al-content rises indicates a move from a single domain to a multidomain system [69]. The Al-content dependency of M_s, H_c, and M_r/M_s is shown in Figure 6b–d. Figure 6b–d's perusal shows that M_s, H_c, and M_r/M_s drop linearly with increasing Al-content, which is consistent with previous findings [70] and may be explained by the following experimental relations:

i. M_s = 52.6–50.2 (Al-content)

ii. H_c = 334.66–328.23 (Al-content)

iii. M_r/M_s = 0.64–0.66 (Al-content)

According to Table 1, the decrease in the Fe^{3+} population on the B-site is responsible for the decrease in saturation magnetization (M_s) with an increase in Al^{3+} concentration. This is in line

with the Neel two-sub-lattice model [71]. The decrease in coercivity (Hc) with the addition of Al is in accordance with the dislocation density values that were obtained (5.6×10^{-14} lines m^{-2} to 8.16×10^{-14} lines m^{-2}). The fluctuation of H_c with grain diameter (D) is shown in Figure 6c (inset), which indicates that the samples under study fall within overlap zones between the single and multidomain regions [72]. Values for M_r. and M_s. vary from 0.15 to 0.48. Randomly orientated uniaxial anisotropic ferromagnetic particles with a mass of 0.5 are represented by $M_r/M_s \sim 0.5$ in the context of the Stoner–Wohlfarth (SW) model for three-dimensional noninteracting random particles [73].

Table 5's analysis reveals that the examined samples' M_r/M_s values, which are below 0.5 and correspond to substantially greater interactions among multidomain grains, vary from 0.15 to 0.48 [74]. As a result, the SW model would be less applicable to the studied samples with Al-content values of 0.5 and 0.75. Consequently, it is not possible to conclude from M_r/M_s values that these samples exhibit uniaxial anisotropy, since it has also been reported that the SW model performs better when applied to randomly orientated uniaxial anisotropic particles in samples with Al-content values of 0.25 [74].

Optical Properties of Synthesized Ferrites

Using UV–visible diffuse reflectance spectroscopy, the optical characteristics of the magnesium–manganese micro ferrite doped with aluminium are investigated. The absorbance spectra of the $Mg_{0.50}Mn_{0.50}Al_{0.75}Fe_{1.25}O_4$ sample are displayed in Figure 7. Bandgap energy (E_g) is computed for the diffused reflectance spectra using the Kubelka–Munk function F(R), and further E_g estimates can be obtained using the Tauc relation [75].

$(R) = (1-R)^2 / 2R$,

$(R)h\nu = (h\nu -)^2$,

where R is the reflectance value, A is the absorption coefficient, and $h\upsilon$ is photon energy. By calculating the intercept values from the graph of $((R)h\nu)^2$, one may estimate the band gap energy. The $Mg_{0.50}Mn_{0.50}Al_{0.75}Fe_{1.25}O_4$ sample has a bandgap energy of 1.64 eV. In a similar vein, $Mg_{0.50}Mn_{0.50}Al_{0.50}Fe_{1.50}O_4$ and $Mg_{0.50}Mn_{0.50}Al_{0.75}Fe_{1.25}O_4$ have band gap energies of 1.67 and 1.70 eV, respectively. Because of its decreased band gap energy, it has been determined that the $Mg_{0.50}Mn_{0.50}Al_{0.75}Fe_{1.25}O_4$ sample may be employed as a photocatalyst for the degradation of MB.

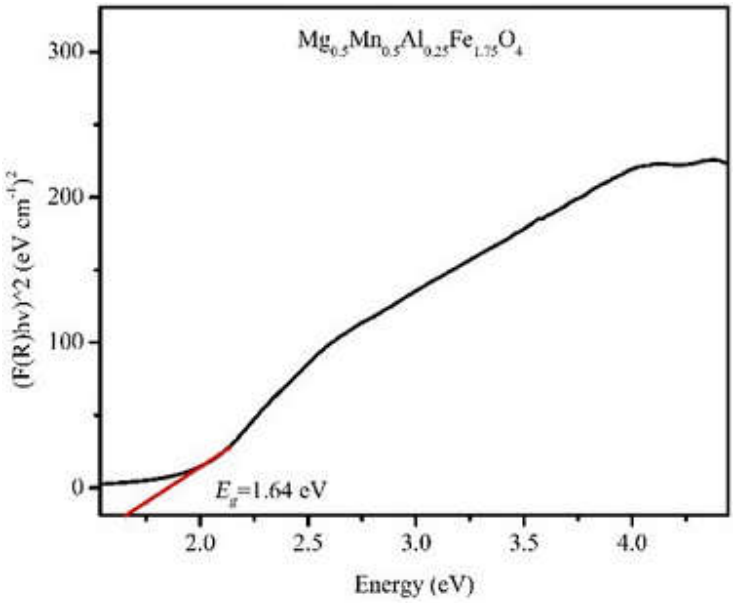

Figure 7 Ultraviolet–visible reflectance spectra of the $Mg_{0.50}Mn_{0.50}Al_{0.25}Fe_{1.75}O_4$ sample (where F(R) = Kubelka–Munk function)

Photocatalytic Dye Degradation of MB Using Synthesized Nano Ferrites in Solar Radiation in Presence of Hydrogen Peroxide

The byproduct of several industrial operations, synthetic dyes has the potential to contaminate natural water supplies. When these dangerous colours break down, a number of carcinogen chemicals are created [76, 77]. An improved oxidation procedure that breaks down the dye's harmful components into carbon dioxide and water can be used to decompose these dyes [78, 79]. Potential possibilities for dye degradation that leave no traces of the pollutant include magnetic spinel ferrites [80, 81]. Photocatalysis uses solar energy to accomplish basic oxidation and reduction activities [82, 83].

By employing electromagnetic radiation to form electron–hole pairs on the photocatalytic surface, spinel ferrite materials can be used as efficient photocatalysts. This electron–hole pair causes the solution to go through reduction and oxidation processes, which in turn results in the production of radicals O_2^{-}• and •OH. The degradation of organic pigment can be aided by these radicals. Moreover, H_2O_2 oxidant can be added to the reaction mixture to promote the generation of reactive oxygen species. These reactions suggest that iron cations combine with H_2O_2 to create extremely reactive •OH radicals. •OH radicals are created when these electrons and holes interact with OH^- or surface-bound H_2O.

The primary active species in the process of photocatalytic degradation are these radicals [84]. One experiment has been detailed for comprehension purposes: 20 mg of $Mg_{0.50}Mn_{0.50}Al_{0.25}Fe_{1.75}O_4$ loading and a combination of 10 ppm MB by varying the H_2O_2 solution were stored in natural light. As indicated in Figure 8, the sample was placed in the UV-visible spectrophotometer after 10 minutes in order to measure the absorbance and determine the percent degradation of MB using a standard formula [57] with regard to contact time. The aforementioned experiment was repeated when the sample was removed from the beaker containing a mixture of MB, synthesized specimen, and hydrogen peroxide after 10 minutes. The dye degradation research of MB employing H_2O_2 specimen in the presence of varying hydrogen peroxide concentrations (mM) is shown in Figure 8. The other two synthesized specimens underwent comparable experiments.

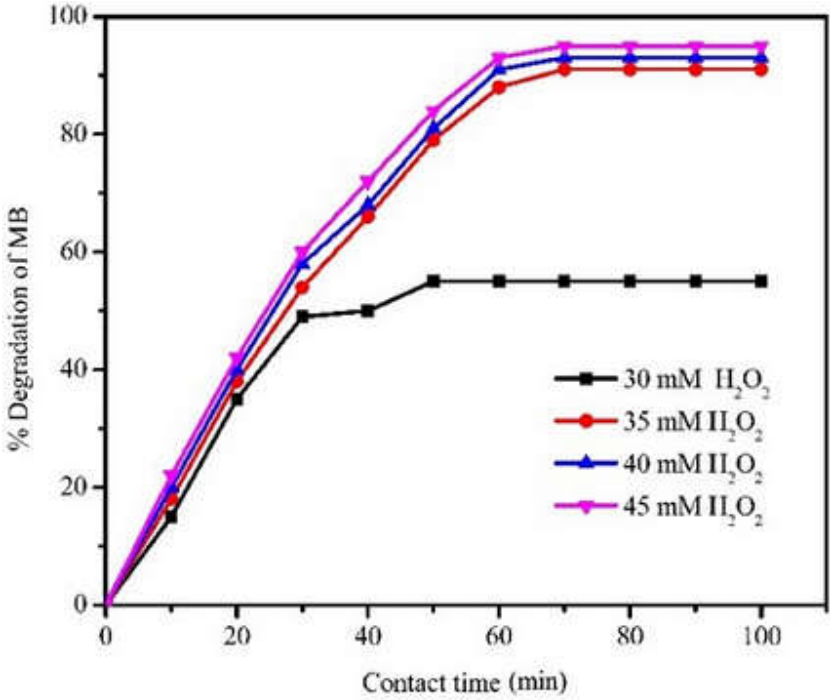

Figure 8 The degradation process of MB dye for the $Mg_{0.5}Mn_{0.50}Al_{0.25}$ $Fe_{1.75}O_4$ catalyst in the presence of H_2O_2

The breakdown of MB dye for the synthesized catalysts in the presence of the minimal amount of H_2O_2 necessary is seen in Figure 9. Table 6 compares the dye degradation studies of MB with varying ferrite loading when the minimal amount of hydrogen peroxide (mM) is present. The minimal concentration of hydrogen peroxide was required due to the bandgap energy of the

synthetic specimen. With a 35 mM H_2O_2 concentration, it was discovered that the $Mg_{0.50}Mn_{0.50}Al_{0.25}Fe_{1.75}O_4$ destroyed the MB (91%) solution in 75 minutes. As a result, it is possible to destroy MB dye in a shorter amount of time by using a certain Al^{3+} concentration in the material under study, and Al addition can aid in this process.

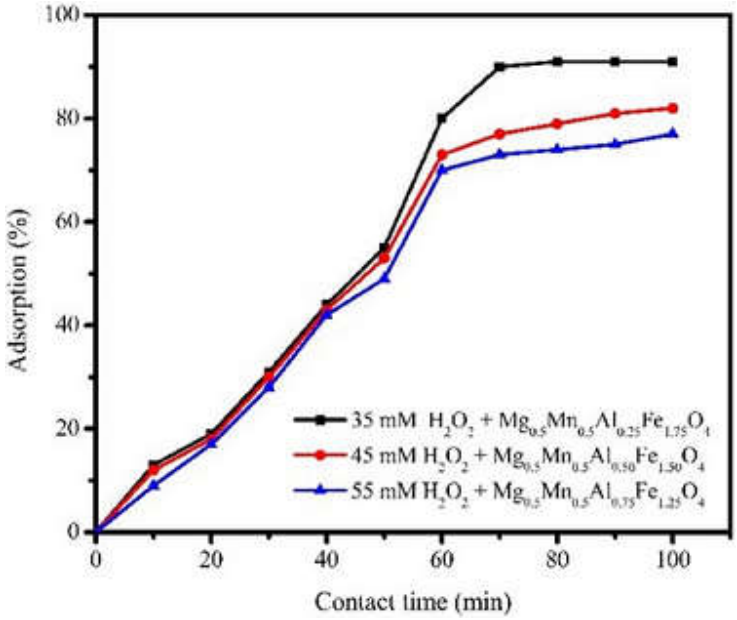

Figure 9 The degradation process of MB dye for the synthesized catalysts in the presence of minimum required H_2O_2

Table 6 Various parameters of the methylene blue dye degradation study

Sample	Minimum required concentration of H_2O_2 (mM)	Contact time (min)	Adsorption (%)
$Mg_{0.50}Mn_{0.50}Al_{0.25}Fe_{1.75}O_4$	35	75	91
$Mg_{0.50}Mn_{0.50}Al_{0.50}Fe_{1.50}O_4$	45	100	82
$Mg_{0.50}Mn_{0.50}Al_{0.75}Fe_{1.25}O_4$	55	100	77

Twenty milligrammes of the $Mg_{0.50}Mn_{0.50}Al_{0.25}Fe_{1.75}O_4$ catalyst were found to be needed in order to accomplish 91% degradation of MB. The breakdown of MB reduced as the catalyst dose rose because of the significant quantity of light scattering that occurred in the system, and it's possible that the catalyst was unable to degrade the MB efficiently [57]. The results of a study on the impact of MB concentration are shown in Figure 11. Here, during the experiment, the H_2O_2

concentration and $Mg_{0.50}Mn_{0.50}Al_{0.25}Fe_{1.75}O_4$ catalyst dose were set at 35 mM and 20 mg, respectively.

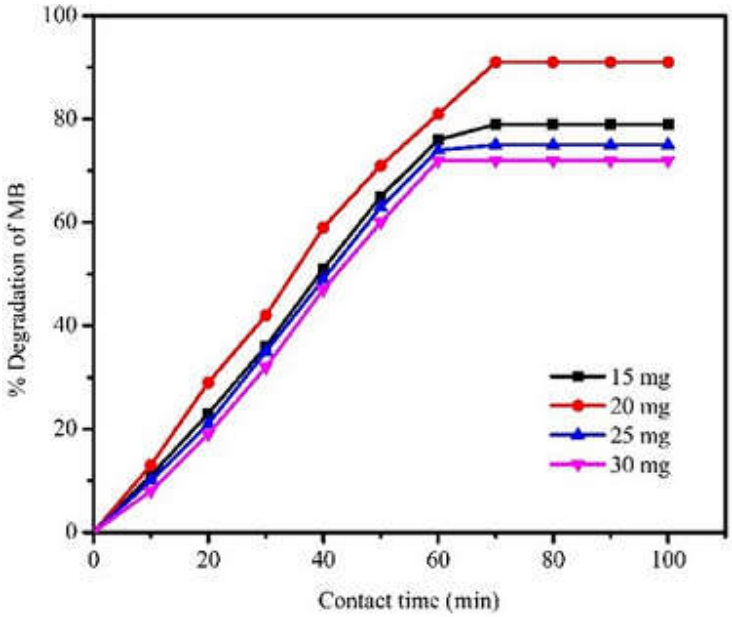

Figure 10 The degradation of MB by variation of catalysts' amount with contact time

As seen in Figure 10, the impact of varying catalyst quantities on the degradation of MB was investigated in relation to the $Mg_{0.50}Mn_{0.50}Al_{0.25}Fe_{1.75}O_4$ catalyst. Here, during the experiment, the concentrations of MB and H_2O_2 were fixed at 10 ppm and 35 mM, respectively.

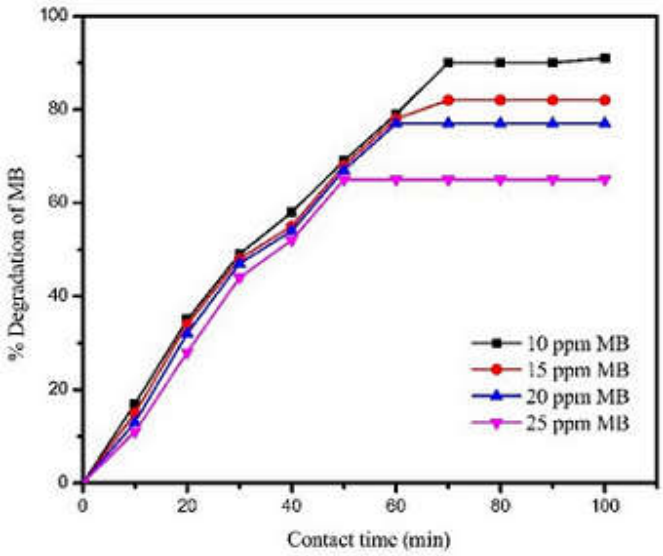

Figure 11 The degradation of MB by variation of methylene blue with contact time

The highest dye degradation was seen in a solution containing 10 parts per million. Because there are fewer active sites for catalysts that would normally cause MB degradation, MB degradation reduces as the ppm solution of dye increases [57].

Conclusion

A modified auto combustion process has been successfully used to synthesize the nano spinel ferrites. XRD and EDAX studies verify the produced nanomagnetic ferrites' purity. All of the generated nanomagnetic ferrites' SEM pictures display their porous structure, which results from a significant quantity of gas released during the production process. Dynamic light scattering tests show the particle sizes of all manufactured nanomagnetic ferrites, which are almost identical to the crystallite sizes found by XRD analysis. Fe^{3+}, Mg^{2+}, and Mn^{2+} are populated on both the A and B sites of the cationic redistribution caused by Al3+ addition, but Al^{3+} ions are entirely populated on the B-site. The structure of the samples has been confirmed by FTIR spectra, and force constants for the spinel ferrites' interstitial sites have been computed. The coercivity values align with the dislocation density, and the decrease in saturation magnetization may be attributed to the cationic redistribution caused by the substitution of nonmagnetic cations (Al^{3+}) for magnetic cations (Fe^{3+}). Al (0.25) has a lower bandgap energy (E_g) than the other two examples. The best specimen for the MB deterioration is Al (0.25). Experiments on hydrogen peroxide-assisted MB dye degradation using micro ferrites loaded in the presence of solar light reveal that the optimal degradation results, up to 91% in 75 minutes, are obtained with an Al-content = 0.25. According to current findings, Al^{3+}-doped Mg–Mn micro ferrites may be able to improve the photocatalytic degradation of MB dye when exposed to sunlight.

Conflicts of Interest

The authors declare no conflicts of interest.

References

1. Desai HB et al., *Ferrites and Multiferroics (Engineering Materials. Springer),* (2021) p 49.
2. Carta D et al., *The J Physic. Chem. C,* 113 (2009) 8605.
3. Kedesdy HH and Tauber A, *J Am Ceram Soc.,* 39 (1956) 425.
4. Gabal MA and Ata-Allah SS, *J Phys Chem Solids.,* 65 (2004) 995.
5. Alvani C et al., *Int J Hydrogen Energy.* 30 (2005) 1407.
6. Zhen L et al., *J Magn Magn Mater.,* 320 (2008) 2672.
7. Hou X et al., *J Alloys Compd.,* 491 (2010) 258.

8. Akhtar MJ and Younas M, *Solid State Sci.,* 14 (2012) 1536.
9. Zhong X et al., (2015) J Ceram Soc Japan. 123:394.
10. Amulya MAS et al., *J Phys Chem Solid.*, 148 (2021) 109661.
11. Naseri MG et al., *J. Magn. Magn. Mater*, 350 (2014) 141.
12. Chen D et al., *Ultrason Sonochem*, 20 (2013) 1337.
13. Thankachan S et al., *J Exp Nanosci*, 8 (2013) 347.
14. Joulaei M et al., *Compos Part B Eng*, 176 (2019) 107345.
15. Sasaki T et al., *J Supercrit Fluids*, 53 (2010) 92.
16. Ali R et al., Ceram *Int*, 40 (2014) 3841.
17. Shedam RM et al., *Int J Self-Propagating High-Temperature Synth*, 26 (2017) 75.
18. Chandradass J and Kim KH, *J Alloys Compd*, 509 (2011) 59.
19. Köferstein R et al., *J Mater Sci*, 48 (2013) 6509.
20. Desai HB et al., Eur Chem Bull, 10 (2021) 186.
21. Bueno AR et al., *J Magn Magn Mater*, 320 (2008) 864.
22. Dhiman M et al., *Integr Ferroelectr*, 202 (2019) 29.
23. Jasrotia R et al., *Phys B Condens Matter,* 569 (2019) 1.
24. Figueroa-Espí V et al., *Colloids Surfaces A Physicochem Eng Asp.*, 387 (2011) 118.
25. Yang H et al., *Biomaterials,* 31 (2010) 3667.
26. Mahmoodi NM, *Desalin Water Treat.*, 53 (2015) 84.
27. Li Z et al., *Advan. Health. Mater*, 2 (2013) 958.
28. Mendes EP et al., *Int J Nanomedicine,* 9 (2014) 3299.
29. Zate MK et al., *J Anal Appl Pyrolysis*, 122 (2016) 224.
30. Wang G et al., *Appl Surf Sci,* 428 (2018) 258.
31. Rahmayeni R et al., *J Dispers Sci Technol,* 0 (2020) 1.
32. Chaudhri A et al., *Chem Phys Imp*, 5 (2022) 100098.
33. Maensiri S et al., *Nanoscale Res Lett,* 4 (2009) 221.
34. Ensafi AA et al., *Anal Sci*, 28 (2012) 705.
35. Malaie K et al., *J Mater Sci Mater Electron*, 29 (2018) 650.
36. Khot VM et al., *J Magn Magn Mater,* 332 (2013) 48.
37. Srivastava V, Sharma YC and Sillanpää M, *Appl Surf Sci*, 338 (2015) 42.
38. Narsimulu D et al.,*Ceram Int*, 42 (2016) 16789.

39. Saeid TF et al., *Nanochem Res*, 4 (2019) 86.
40. Patil JY et al., *Curr Appl Phys*, 12 (2012) 319.
41. Deraz NM, *Egypt J Chem*, 61 (2018) 531.
42. Hafiz HM and Moyo T, *J Supercond Nov Magn*, 28 (2015) 955.
43. Desai HB et al., *Bionanoscience*, 12 (2022) 62.
44. Khan I et al., *Water*, 14 (2022) 242.
45. Cheng J et al., *Omega,* 5 (2020) 5389.
46. Al Bassami NS, Mansour SF, *Appl. Phys. A*, 127 (2021) 38.
47. N. Y. Mostafa et al., *Appl. Phys. A*, 124 (844) (2018) 1.
48. M. Y. Naz et al., *Appl. Phys. A.*, 127(491) (2021) 1.
49. S. Pan et al., *Appl. Phys. A,* 125(88) (2019) 1.
50. Kambale RC et al., *J Alloys Compd,* 491 (2010) 372.
51. Bertaut, E.F.: *Etude de la nature des ferrites spinelles. Comptes Rendus Hebdomadaires des Seances de I'Academie des Sciences*, 230 (1950) 213.
52. Tanna AR, Joshi HH, *Inter J Phy and Mathe Sci* 7(3) (2013) 334.
53. Satalkar M and Kane SN, *J Phys Conf Ser*, 755 (2016) 012050.
54. Tanna AR, Sosa KM and Joshi HH, *Mater Res Express*, 4 (2017) 9393.
55. Soibam I and Mani AD, *Mater Today Proc*, 5 (2018) 2064.
56. Thummer KP, Tanna AR and Joshi HH, *AIP Conf Proc*, 1837 (2017) 1
57. Chauhan BS, Kumar R, Jadhav KM, Singh M, *J. Magn. Magn. Mater.,* 283 (2004) 71.
58. Shahzadi K et al.,*Opti and Qua Ele,* 52 (2020) 190.
59. Islam K et al., *Nanomaterials,* 10 (2020) 2297.
60. Raje Shaikh BB and Chishty SQ, *J Mater Sci: Mater Electron,* 19 (2021) 2399.
61. Manouchehri S, Benehi STM, Yousefi MH, *J. Supercond. Novel Magnetism*, 29 (2016) 2179
62. A. Fairweather, F.F. Roberts, A.J.E. Welch, Ferrites, Reports Prog. Phys. 15 (1952) 306,
63. Kolhatkar A.G et al., Int. J. Mol. Sci. 14 (2013), 15977–16009.
64. Stoner E.C., Wohlfarth E.P. Philos. Trans. R. Soc. London. 240 (1948) 599–642.
65. Muthuselvam I. P., Bhowmik R. N., J. Magn. Magn. Mater. 322 (2010) 767-776.
66. Kane S. N., Satalkar M. J., Mater. Sci. 52 (2017) 3467–3477.
67. Sheng S et al., *Int J Environ Res Public Health*, 15 (2018) 35.
68. Venkatesh S, Venkatesh K and Quaff AR, *J Appl Res Technol.,* 15 (2017) 340.

69. Jamee R and Siddique R, *Eur J Microbiol Immunol*, 9 (2019) 114.
70. Sun JH et al., *J Hazard Mater*, 153 (2008) 187.
71. Jani P, Desai H, Madhukar BS and Tanna A, *Mater Res Innov,* 26 (2021) 189.
72. Wang WY and Ku Y., *Water Res*, 40 (2006) 2249.
73. Ince NH and Tezcanlí G, *Dye Pigment*, 49 (2001) 145.
74. Jamil TS, Roland H, Michael H and Jens-Uwe R, *J Water Process Eng*, 18 (2017) 159.
75. Madhukara Naik M et al., *Microchem J*,146 (2019) 1227.